

1 *This is the peer reviewed version of the following article: -Near UV-irradiation of CuO_x*
2 *impregnated TiO₂ provides active species for hydrogen production through methanol*
3 *photoreforming- ChemCatChem 2019, 11, 4314 – 4326, which has been published in final form at*
4 <https://doi.org/10.1002/cctc.201900818>. *This article may be used for non-commercial purposes in*
5 *accordance with Wiley Terms and Conditions for Use of Self-Archived Versions*
6

7 **Near UV-irradiation of CuO_x impregnated TiO₂ provides active**
8 **species for hydrogen production through methanol photoreforming**
9

10 Giuseppe Vitiello^{1,2}, Laura Clarizia^{1,*}, Wael Abdelraheem^{3,4}, Serena Esposito⁵, Barbara Bonelli⁶,
11 Nicoletta Ditaranto⁷, Alessandro Vergara⁸, Mallikarjuna Nadagouda⁹, Dionysios D. Dionysiou³,
12 Roberto Andreozzi¹, Giuseppina Luciani^{1,*}, Raffaele Marotta¹
13

14 ¹ Department of Chemical, Materials and Production Engineering (DICMaPI), University of Naples
15 Federico II, p.le Tecchio 80, 80125 Naples, Italy.

16 ²CSGI - Center for Colloids and Surface Science, via della Lastruccia 3, 50019 Sesto Fiorentino (FI),
17 Italy.

18 ³Environmental Engineering and Science Program, Department of Chemical and Environmental
19 Engineering, 705 Engineering Research Center, University of Cincinnati, Cincinnati, OH 45221-
20 0012, United States.

21 ⁴Department of Chemistry, Faculty of Science, Sohag University, 82524 Sohag, Egypt.

22 ⁵Department of Civil and Mechanical Engineering, University of Cassino and South of Lazio, Via G.
23 Di Biasio 43, 03043 Cassino (FR), Italy.

24 ⁶Department of Applied Science and Technology and INSTM Unit of Turin-Polytechnic, Polytechnic
25 of Turin, C.so Duca degli Abruzzi 24, I-10129 Turin, Italy.

26 ⁷Department of Chemistry, University of Bari Aldo Moro, via Orabona 4, 70125 Bari, Italy.

27 ⁸Department of Chemical Sciences, University of Naples Federico II, Complesso di Monte S. Angelo,
28 80126 Naples, Italy.

29 ⁹Department of Mechanical and Materials Engineering, Wright State University, Dayton, Ohio
30 45324, United States.

31 *Corresponding Authors: Giuseppina Luciani (giuseppina.luciani@unina.it), Laura Clarizia
32 (laura.clarizia2@unina.it)

33

34

35

36 **Abstract**

37 Copper doped-TiO₂ (P25) nanomaterials have been intensively studied as promising catalysts for H₂
38 production by photo-reforming of selected organic compounds. However, the role of copper oxidation
39 states on the improvement of photocatalytic activity is still debated. In this work, CuO_x-impregnated
40 P25-TiO₂ catalysts were used for photocatalytic production of hydrogen from methanol. Copper
41 species/oxidation states in the as-prepared catalysts were identified, and their transformations during
42 the photocatalytic process were investigated. For this purpose, H₂ production rates were correlated to
43 physico-chemical properties of Cu-impregnated P25-TiO₂ samples, both before and after
44 photocatalytic process, by means of Raman, X-Ray Diffraction, Electron Paramagnetic Resonance
45 spectroscopy, X-Ray Photoelectron Spectroscopy, Temperature-Programmed Reduction and High
46 Resolution Transmission Electron Microscope techniques. Results revealed the presence of both
47 Cu₂O and CuO deposits on the samples surface after calcination. Notably, under near-UV irradiation,
48 copper(I, II) oxides undergo a partial dissolution process, followed by reduction to metallic copper
49 Cu_(s) by photogenerated electrons, boosting H₂ production rate. In particular, the fraction of highly
50 dispersed CuO particles must be mainly involved in this process, thus accounting for an improved H₂
51 evolution. Our findings indicate that both Cu₂O and Cu_(s) act as co-catalysts for H₂ generation, yet
52 by different mechanisms. Overall this study, lies the basis to enhance catalytic performance of red-
53 ox active systems through UV-irradiation approach.

54

55 *Keywords:* copper-based TiO₂, hydrogen production, photoreforming, photocatalysis, methanol.

56

57 **1. Introduction**

58 Limited availability of fossil fuels as well as their environmental impact has prompted scientific
59 research towards cleaner and renewable energy sources. In this scenario, sunlight-driven H₂
60 production by either photo-reforming or water photo-splitting holds a great promise [1,2]. However,
61 photoreforming-based technologies have far from practical application and poor efficiencies [1].
62 Thus, improvement and optimization of photocatalytic systems are crucial tasks to make this
63 technology feasible [3]. Indeed, photocatalysts with appropriate band-gap and adequate stability for
64 either organic photo-reforming or water-splitting under visible light irradiation with suitable energy
65 efficiencies are still unavailable, and their development is considered a significant challenge in
66 photocatalysis research.

67 Even though titanium dioxide in P25 form (80:20 w/w anatase:rutile) is considered one of the most
68 promising commercial material for photocatalytic processes, it shows significant limitations, such as
69 fast electron/hole recombination and absorption/activity restricted to the UV region due to its wide
70 bandgap [4,5]. Among the various methods employed for improving TiO₂ features, doping with noble
71 metals (Au, Pt, Pd) acting as co-catalysts has proven to be effective to enhance the photo-efficiency
72 of titanium dioxide [3,6-8].

73 Alternatively, doping with transition metal ions such as Cu, Fe, Co, Ni is a cheaper promising option
74 [4,7]. The advantages of adopting these species lie in their behavior as electron scavengers, thus
75 limiting charge recombination [7]. In particular, copper loaded-P25 nanomaterials, prepared by
76 impregnation method, have been proposed as promising catalysts for photo-reforming [9-11].
77 Although several studies have investigated the effect of copper loading on P25 nanoparticles for the
78 photocatalytic hydrogen generation through reforming of organics (Table 1), the effect of copper
79 oxidation state on the improvement in photocatalytic activity, is not yet entirely clarified. Different
80 conflicting opinions have been provided on synergistic effects of active copper species in photo-
81 catalytic reactions.

82

83 **Table 1** - Selected research papers devoted to testing Cu/P25 photocatalysts, prepared by
 84 impregnation method, in various photocatalytic processes.

| Precursor | Calcination temperature (°C) | Cu oxidation state | Diagnostic technique | Application | Ref. |
|---|------------------------------------|-----------------------------------|-------------------------|--|------|
| $\text{Cu}(\text{NO}_3)_2 \times 3\text{H}_2\text{O}$ | 300 – 500 for 0.5 h | CuO | TPR, XRD | Hydrogen production | [12] |
| $\text{Cu}(\text{NO}_3)_2 \times 2.5\text{H}_2\text{O}$ | 300 for 5 h (in air) | CuO | TPR | CO oxidation | [13] |
| $\text{Cu}(\text{NO}_3)_2 \times 2.5\text{H}_2\text{O}$ | 300 for 5 h (in air) | CuO/Cu ₂ O | TPR, XRD, XPS, Raman | CO oxidation | [14] |
| $\text{Cu}(\text{NO}_3)_2$ | 400 for 16 h (in air) | CuO | TPR, XRD, FTIR | Hydrogenation of 1,3-cyclooctadiene | [15] |
| $\text{Cu}(\text{CH}_3\text{COO})_2 \times \text{H}_2\text{O}$ | 250 for 4 h (in air) | Cu ²⁺ /Cu ⁺ | TPR, XPS, FTIR | Hydrogenation of crotonaldehyde | [16] |
| $\text{Cu}(\text{NO}_3)_2$ | 400 for 1h (in Helium) | CuO/Cu ₂ O | TPR, XPS, FTIR, | CO oxidation | [17] |
| $\text{Cu}(\text{NO}_3)_2$ | 300 – 500 for 5 h | CuO/Cu ₂ O | DRS, XPS, FTIR | Hydrogen production | [18] |
| $\text{Cu}(\text{NO}_3)_2 \times 3\text{H}_2\text{O}$ | 300 for 0.5 h (in air) | CuO/Cu ₂ O | XPS, XRD | Hydrogen production | [19] |
| $\text{Cu}(\text{CH}_3\text{COO})_2 \times \text{H}_2\text{O}$ or $\text{Cu}(\text{NO}_3)_2$ | 500 – 600 for 1 h (in Argon) | CuO/Cu ₂ O | XRF, XRD | Acetic acid decomposition, hydrogen production | [20] |
| $\text{Cu}(\text{NO}_3)_2 \times 3\text{H}_2\text{O}$ | 400 for 2 h | CuO | XANES, EXAFS | Methylene blue degradation | [21] |
| $\text{Cu}(\text{NO}_3)_2$ | 350 for 4 h (in air) | CuO | XRD | Hydrogen production | [22] |
| $\text{Cu}(\text{NO}_3)_2 \times 3\text{H}_2\text{O}$ | 350 for 2 h (in air) | Cu ₂ O | XPS, XRD | Hydrogen production | [23] |

| | | | | | |
|---|-------------------------|---|----------------------|----------------------------|------|
| $\text{Cu}(\text{NO}_3)_2$ | 100 – 600 n.r. | CuO | XPS, XRD | Hydrogen production | [24] |
| $\text{Cu}(\text{NO}_3)_2$ | 350 for 4 h (in air) | CuO | XRD | Hydrogen production | [25] |
| $\text{Cu}(\text{NO}_3)_2 \times 3\text{H}_2\text{O}$ | 450 for 4 h (in air) | CuO | XPS, XRD | Hydrogen production | [26] |
| $\text{Cu}(\text{NO}_3)_2 \times 3\text{H}_2\text{O}$ | 450 for 4 h (in air) | CuO , $\text{Cu}_x\text{Ti}_{1-x}\text{O}_2$ | XRD, XANES, EXAFS | Hydrogen production | [27] |
| CuCO_2CH_3 | 400 for 1h (in air) | Cu_2O , CuO | XPS, XRD, DRUV | Gallic Acid degradation | [28] |

85

86 Several studies report that Cu_2O species are responsible for enhanced photocatalytic H_2 production
87 from water [6, 7, 18, 29]. On the other hand, the presence of CuO was argued by different authors to
88 be responsible for the enhanced separation of photoinduced electrons and holes [3,22, 24, 25].
89 Similarly, Valero et al. proposed that easily reduced Cu^{2+} species could be responsible for higher
90 $\text{Cu}/\text{P25}$ photoactivity [30]. Other scientific studies also ascribe the improved photocatalytic activity
91 of $\text{Cu}/\text{P25}$ systems to the presence of finely dispersed and easily reducible CuO_x (Cu^+/Cu) species on
92 the TiO_2 surface [31]. Such widespread variability in scientific conclusions is due to an intrinsic
93 complexity of materials during photocatalytic experiments, along with different impregnation
94 procedures for copper doping of P25 resulting in mixed oxidation states of copper on the catalyst
95 surface. Typically, copper exists in different oxidation states ($\text{Cu}_{(s)}$, Cu^+ , Cu^{2+}), that can change under
96 UV-irradiation [32-34].
97 In this scenario, the present paper aims at elucidating the nature of copper species in Cu/TiO_2
98 photocatalysts prepared via impregnation-calcination method. Moreover, evolution of copper species
99 under UV-irradiation during phot-reforming process was investigated, in order to clearly identify the
100 active species involved in H_2 production . Hydrogen production rates were compared and integrated

101 with a detailed physico-chemical characterization of the catalyst before and after the photo-catalytic
102 process, through a combined approach of complementary techniques, including X-Ray diffraction
103 (XRD), X-Photoelectron Spectroscopy (XPS), Raman and Electron Paramagnetic Resonance (EPR)
104 Spectroscopies, Scanning Electron Microscopy (SEM) and High Resolution Transmission Electron
105 Microscopy (HR-TEM) as well as Temperature Programmed Reduction (TPR) analysis. This study
106 is expected to deliver significant insights on the molecular factors responsible for the improved
107 photocatalytic activity of Cu-based TiO₂ materials, thus providing critical guidelines for the design
108 of new copper doped photocatalysts for UV-solar photoreforming.

109

110 **2.Experimental procedures**

111 *2.1 Materials*

112 Methanol (99.8% v/v), P25-TiO₂ (80:20 anatase:rutile), sodium nitrite (NaNO₂, purity ≥97.0%) used
113 as filter and cupric nitrite hydrate (Cu(NO₃)₂·3H₂O, purity 99.9%) were purchased from Sigma
114 Aldrich. Bi-distilled water was used for the preparation of the reacting mixtures.

115

116 *2.2 Cu/P25 material preparation*

117 Copper (0.5, 3, 6, 10 and 16 wt %) was loaded on P25-TiO₂ by impregnation method [18]. For each
118 Cu-modified P25-TiO₂ sample (Cu/P25), a required amount of P25-TiO₂ was dispersed in Cu(NO₃)₂
119 aqueous solution. Excess water was evaporated to dryness with slow heating rate and constant
120 stirring. The samples were dried at 110 °C and then calcined under nitrogen atmosphere for 5h at
121 different temperatures ranging between 150 °C and 550 °C.

122

123 *2.3 Photocatalytic runs*

124 Photocatalytic runs were carried out in triplicate in an annular glass batch reactor (V=300 mL)
125 covered with a layer of aluminum foil. The reactants and nitrogen gas were fed to the reactor through

126 its top inlet hole, while collection of outflow liquid and gaseous samples was performed at the bottom
127 hole of the reactor at different reaction times. The reactor has been endowed with a high-pressure
128 mercury vapor lamp (input power: 125 W) manufactured by Helios Italquartz emitting in both
129 ultraviolet and visible range.

130 The lamp had ultraviolet emission peaks at 305, 313, and 366 nm corresponding to irradiances of
131 2.23×10^{-6} , 2.76×10^{-6} and 3.37×10^{-6} (E/s). The visible emission peaks at 405, 408, 436, and 546,
132 corresponded to irradiances of 6.18×10^{-7} , 1.41×10^{-7} , 1.03×10^{-6} , and 1.16×10^{-6} E/s, respectively. The
133 reactor was cooled at 25 °C during each run by means of a thermostatic bath (Falc GTR 90).

134 In order to evaluate the response of the photocatalytic system under visible light irradiation, during
135 the experimental runs water in the cooling jacket was replaced by 1M NaNO₂ solution absorbing
136 ultraviolet radiation, as reported elsewhere [35]. The pH of the solution was monitored by means of
137 an Orion 420A_p pH-meter (Thermo).

138 In order to avoid the undesired reaction of dissolved oxygen with photogenerated electrons, before
139 starting the photocatalytic runs, a nitrogen stream was bubbled into the solution for 30 minutes for
140 removing atmospheric oxygen. Moreover, throughout the experiments, nitrogen was continuously fed
141 at a flow rate (Q_{N_2}) of 0.3 L/min to prevent any entrance of air into the reactor. For each run, fixed
142 amounts of photocatalysts and methanol (10% v/v) were added to 300 mL of aqueous solution; the
143 resulting suspension was sonicated and fed into the batch reactor under magnetic stirring. The liquid
144 samples, collected at different reaction times, were quickly filtered on regenerated cellulose filters
145 (pore diameter 0.20 μm, Scharlau) and the filtrate was used to measure dissolved copper and formic
146 acid concentrations. The gaseous samples were recovered from the reactor outlet in Tedlar gas
147 sampling bags and then used to evaluate hydrogen concentration.

148 Dissolved copper concentration was measured by means of a colorimetric method using an analytical
149 kit (Macherey–Nagel) based on oxalic acid bis-cyclohexylidene hydrazide (cuprizone). A UV/Vis
150 spectrometer (Cary 100 UV–Vis, Agilent) has been employed for the measurements at a wavelength
151 of 585 nm.

152 Hydrogen concentration was measured by a gas-chromatograph (Agilent 7820A) equipped with a
153 HP-PLOT Molesieve 5A column (Agilent) and a TCD detector using argon as carrier gas. During
154 the experiments, the radiation transmitted by the reactor was measured by means of a radiometer (not
155 shown in the figure) in the range 315-400 nm and 401-1100 nm.

156

157 *2.4 Physico-chemical characterization of the Cu/P25 nanomaterials*

158 A physico-chemical investigation on Cu/P25 nanomaterials was performed by using a combined
159 approach of different analytical techniques, such as High Resolution Transmission Electron
160 Microscope (HR-TEM, X-Ray Diffraction (XRD), Temperature-Programmed Reduction (TPR),
161 Raman, Electron Paramagnetic Resonance (EPR), and X-Ray Photoelectron Spectroscopy (XPS)
162 spectroscopies. Also, the specific surface area (S_{BET}) of catalysts was also determined through BET
163 porosimetry. Finally, H₂ Temperature Programmed Reduction (H₂-TPR) analysis was also
164 performed. The characterization was specifically focused on Cu(3%)/P25 and Cu(10%)/P25 catalysts
165 before and after their use in the photo-reforming process.

166 BET analysis allowed determining the specific surface area (S_{BET}), that was evaluated by generating
167 seven-point isotherms at 77 K for N₂ adsorption (Autosorb-1, Quantachrome) using the charred
168 sample capable of providing a specific surface area equal to 5 m² in the sample cell.

169 Raman spectra of the prepared catalysts were performed by using a confocal Raman Microscope
170 (Jasco, NRS-3100). Both the 514 nm line of an air-cooled Ar⁺ laser (Melles Griot, 35 LAP 431-220)
171 and the 647 nm line of a water-cooled Kr⁺ laser (Coherent Innova 302C) were used. The laser line
172 was injected into an integrated Olympus microscope and focused to a spot size of approximately 2
173 mm by using a 100× or 20× objective. A holographic notch filter was used to reject the excitation
174 laser line. Raman scattering was collected by using a Peltier-cooled 1024×128 pixel CCD photon
175 detector (Andor DU401BVI). For most systems, it took 60s to collect a complete data set. XRD
176 measurements were performed using a PANalytical diffractometer with a nickel filter and Cu K α
177 radiation.

178 EPR experiments were carried out by means of X-band (9 GHz) Bruker Elexys E-500 spectrometer
179 (Bruker, Rheinstetten, Germany), equipped with a super-high sensitivity probe head. Solid samples
180 were transferred to flame-sealed glass capillaries which, in turn, were coaxially inserted in a standard
181 4 mm quartz sample tube. Measurements were performed at room temperature. The instrumental
182 settings were as follows: sweep width, 1500 G; resolution, 1024 points; modulation frequency, 100
183 kHz; modulation amplitude, 1.0 G. 16 scans were accumulated to improve the signal-to-noise ratio.
184 TPR measurements were carried out in a laboratory flow apparatus, using a 5% H₂/Ar ($Q= 20 \text{ cm}^3/$
185 min), with a heating rate of 10 °C/min up to 800 °C. The sample (60 mg) was loaded in a quartz
186 down-flow cell with a K thermocouple in close contact with the sample.

187 The nanoparticles morphology and crystallinity were investigated using a JEOL (JEM-2010F) high
188 resolution-transmittance electron microscope (HR-TEM) with the filed transmission of 200 kV. To
189 prepare the samples for HR-TEM, the catalysts were suspended in ethyl alcohol and sonicated for 45
190 min, then fixed on a Lacy Carbon grid (LC300, EMS) by the drop-casting method.

191 X-ray Photoelectron Spectroscopy (XPS) analysis was performed with a Versa Probe II Scanning
192 XPS Microprobe spectrometer (Physical Electronics GmbH). The measurements were done with a
193 monochromatized AlK α source (X-ray spot 100 μm), at a power of 24.4 W. Wide scans and detailed
194 spectra were acquired in Fixed Analyzer Transmission (FAT) mode with a pass energy of 117.40 eV
195 and 29.35 eV, respectively. An electron gun was used for charge compensation (1.0V 20.0 μA). All
196 binding energies were referenced to C1s at 284.8 \pm 0.1 eV for adventitious hydrocarbon. Data
197 processing were performed using MultiPak software v. 9.5.0.8.

198 There is no need to add any description because XAES information are derived from XPS
199 experiments.

200 **3.Results and Discussion**

201 **3.1 Photocatalytic runs**

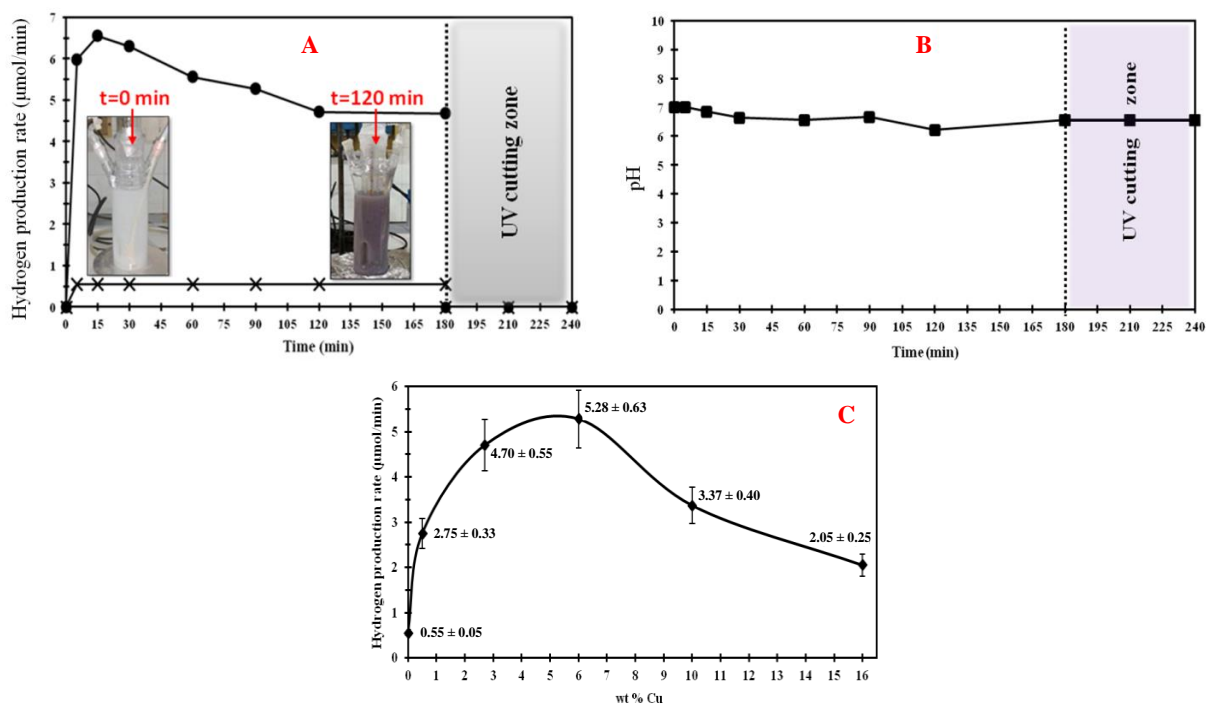
202 *3.1.1 Effect of photocatalyst copper content on H₂ generation*

203 P25-based samples with different copper weight percentages, in the range 0.5-16 wt%, were tested
204 for hydrogen generation through photoreforming of methanol. Fig. 1A shows H₂ production rate of
205 Cu(3%)/P25 after calcination at 350 °C; this trend, approaching a plateau within about 120 minutes,
206 is representative of all compositions. During the photocatalytic run, the suspension turned from light
207 teal to deep indigo, thus suggesting that a change in copper oxidation state occurred under UVA
208 irradiation [19]. After 180 minutes of reaction, UVA radiation was cut off by inserting a NaNO₂
209 solution (1 M) into the cooling system, as described in the Experimental section. Such procedure
210 allowed to test the photocatalytic activity under merely visible light irradiation. No hydrogen
211 generation was recorded for any catalysts tested under merely visible light irradiation, thus indicating
212 that such system are active only under UV irradiation. Furthermore, hydrogen production rates were
213 remarkably higher than values obtained over bare P25-TiO₂ calcined under inert atmosphere at 350
214 °C for 5 hours (0.55 μmol/min) and comparable to the values measured by Jung et al. by using H₂-
215 treated Cu/P25 samples [19].

216 Figure 1B depicts the change in solution pH during the photoreforming run. There was no changes in
217 pH, that kept constant at about 6.5 throughout the experiment. Furthermore, no trace of dissolved
218 copper was appreciated throughout the experiment, thus suggesting a high stability of the
219 photocatalyst.

220 Fig. 1C shows hydrogen production rate as a function of copper content. A non-monotonic trend was
221 appreciated, with catalysts containing 3% and 6% weight percentages of copper displaying
222 comparable similar values of hydrogen production rate, which were also the highest recorded.

223 All Cu/P25 systems showed higher absorption capability than bare P25-TiO₂ both in the UV and
224 visible range (Figure S1A-B), although this did not result in a catalytic activity of the Cu-doped
225 catalyst under visible light irradiation.



226
 227 **Figure 1 - Panel A:** Hydrogen production rate over (●) Cu(3%)/P25 and (×) bare P25-TiO₂, both
 228 calcined under inert atmosphere at 350 °C for 5 hours. After 180 minutes of reaction, UVA radiation
 229 has been cut off by inserting 1 M NaNO₂ solution into the cooling system. Catalysts load =150 ppm.
 230 [CH₃OH]₀ = 2.47 M. T=25 °C. P=1atm. The insets represent the colour suspension with Cu(3%)/P25
 231 before and after 120 min of reaction. **Panel B:** Solution pH throughout the photoreforming run over
 232 Cu(3%)/P25 catalyst calcined under inert atmosphere at 350 °C for 5 hours. After 180 minutes of
 233 reaction, UVA radiation was cut off by inserting 1M NaNO₂ solution into the cooling system.
 234 Cu(3%)/P25 catalyst load=150 ppm. [CH₃OH]₀ = 2.47 M. T=25 °C. P=1 atm). For each value, 12%
 235 error was considered, based on the results of a reproducibility photoreforming run performed over
 236 Cu(3%)/P25 calcined at 350 °C. **Panel C:** Plateau values of hydrogen production rate recorded over
 237 P25-TiO₂ catalysts calcined under inert atmosphere at 350 °C for 5 hours with different copper
 238 content. Weight percentages of copper: 0.5%, 3%, 6%, 10%, 16%.Cu/P25-TiO₂ catalysts load=150
 239 ppm. [CH₃OH]₀ = 2.47 M. T=25 °C. P=1 atm.

240
 241
 242 *3.1.2 Effect of photocatalyst calcination temperature on H₂ generation*

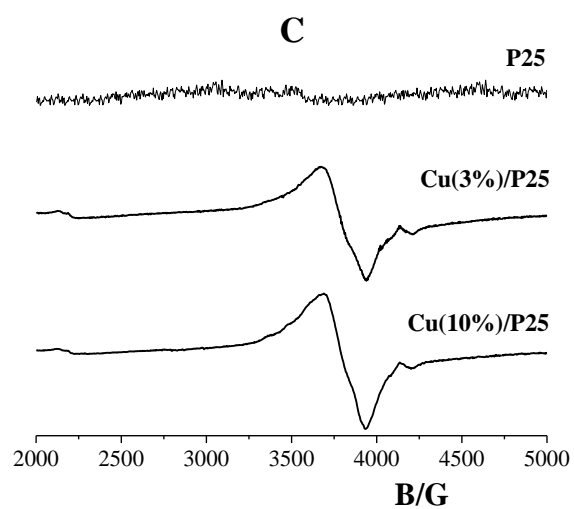
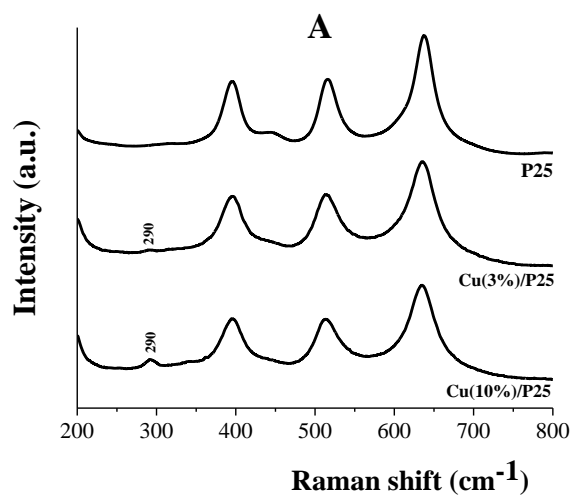
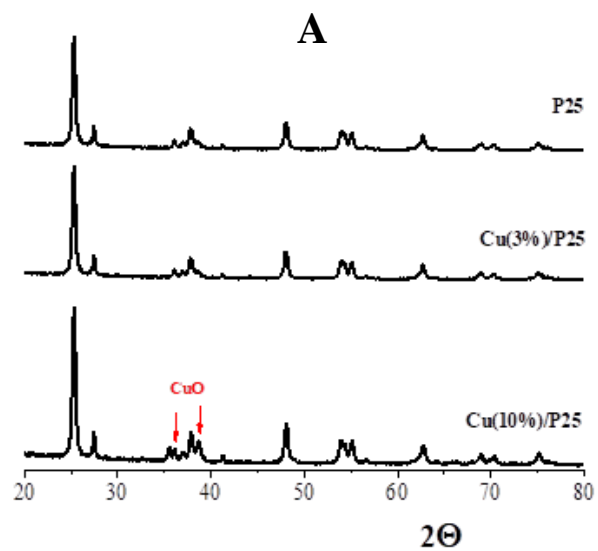
243 Cu/P25 samples calcined under inert N₂ atmosphere for 5 hours at different temperatures were tested
 244 for hydrogen generation through photo-reforming of methanol. Calcination temperatures were
 245 investigated in the range of 150-550 °C (Figure S2, Supplementary Information). Similar values of
 246 hydrogen generation rates were achieved by using catalysts calcined at 150-350 °C, though, further
 247 increase in calcination temperature showed detrimental results in terms of photoefficiency for
 248 hydrogen generation. Once again, no hydrogen evolution was recorded by excluding UV irradiation
 249 for all catalysts tested.

250 **3.2 Characterization of the fresh photocatalysts**

251 Detailed physico-chemical characterizations of Cu/P25 samples were carried, before and after
252 photocatalytic experiments, in order to investigate changes in catalysts' properties upon use for H₂
253 production under near-UV irradiation. In particular, copper oxidation states in Cu deposited species
254 on P25 surface were assessed both before and after photocatalytic experiment with the aim of
255 revealing their role in the enhancement of photocatalytic H₂ production.

256 The measured values of BET surface specific area (S_{BET}) for Cu/P25 catalysts calcined at different
257 temperatures or with different Cu loads are summarised in Table S1 (Supplementary Information).
258 No particular changes were observed before and after use (data not shown), but a significant decrease
259 in the surface area was recorded for the catalyst calcined at 550 °C, likely due to some aggregation
260 phenomenon. Specifically, the highest surface area of 41 m²/g was recorded for Cu(3%)/P25 calcined
261 at 350 °C.

262 XRD spectra were collected in order to assess crystalline properties in the catalysts. Figure 2A shows
263 XRD spectra of bare P25, fresh Cu(3%)/P25 and Cu(10%)/P25 calcined at 350 °C for 5h. Peaks of
264 anatase and rutile structures appeared in all samples. Furthermore, XRD profiles of the fresh
265 Cu(3%)/P25 samples did not show any diffraction peaks of CuO_x species, in agreement with the low
266 amount of Cu. On the contrary, XRD spectrum of Cu(10%)/P25 sample highlighted two diffraction
267 peaks at about 36.5° and 38.5°, displaying the presence of CuO [19]. Comparison of the peak
268 intensities of rutile and anatase revealed the typical composition of P25 samples that was not altered
269 neither by Cu impregnation (Figure 2A). Furthermore, no relevant changes in peak position and
270 intensity were appreciated the XRD patterns of samples treated up to 450 °C (Figure S3), revealing
271 that thermal treatment did not significantly alter the samples crystalline structure.

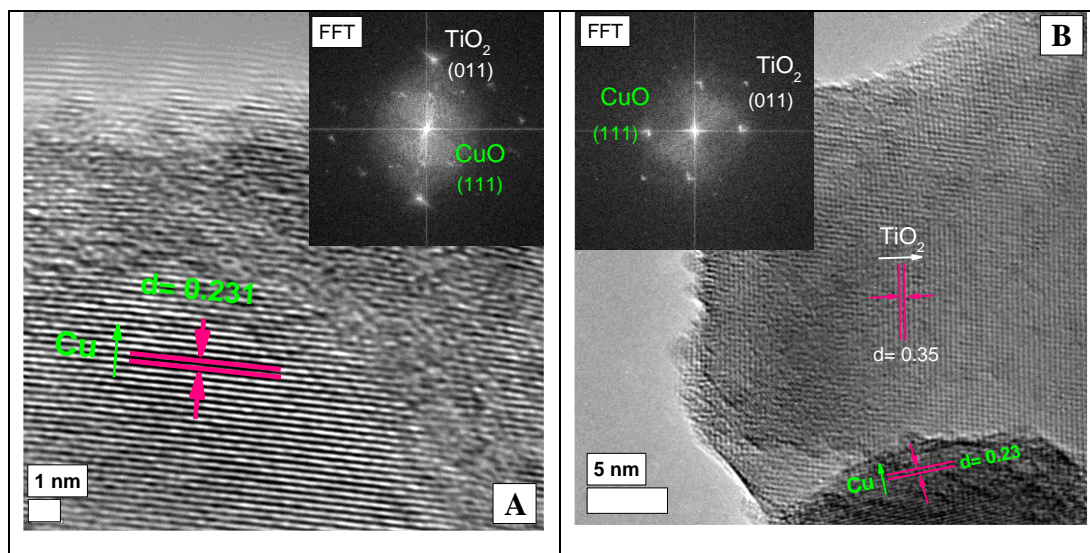


272

273 **Figure 2** – XRD patterns (**panel A**), Raman spectra (**panel B**) and normalized EPR spectra (**panel**
 274 **C**) of bare P25, fresh Cu(3%)/P25 and Cu(10%)/P25 calcined at 350 °C for 5h.
 275

276 Raman and EPR spectra were also recorded in order to define the oxidation state of copper
277 impregnated on the P25 surface for materials before their use (Figure 2B-C). Concerning the fresh
278 Cu/P25 catalyst, Raman spectra were recorded on Cu(3%)/P25 and Cu(10%)/P25 samples (Figure
279 2B) also compared to P25 as reference material. Both catalysts showed a peak at 290 cm^{-1} , which is
280 ascribable to the Raman band of CuO. Although it is usually detected around 279 cm^{-1} , and is
281 associated to an A_g mode [37], the upshift in wavenumbers observed in our experiments compared to
282 pure CuO can occur either due different structuring or to interactions with the hosting matrix (herein
283 TiO_2). On the other hand, the typical most intense Raman band of Cu_2O and corresponding to the
284 second order overtone $2\Gamma_{12^-}$ (216 cm^{-1}) [36] was never visible in any analysed catalyst (Figure 2B).
285 The presence of cupric species in pre-used (fresh) Cu(3%)/P25 and Cu(10%)/P25 catalysts was also
286 confirmed by EPR spectra (Figure 2C) showing an asymmetric signal for both samples at a g-factor
287 of ~ 2.0800 , which is larger than the g-value of free electron $g_e = 2.0023$ and is related to the presence
288 of Cu^{2+} in the distorted octahedral coordination of TiO_2 [38]. The broadness of the EPR spectra
289 indicates the presence of dipolar interaction among neighboring Cu^{2+} ions that leads to the increase
290 in the width of the EPR signal.

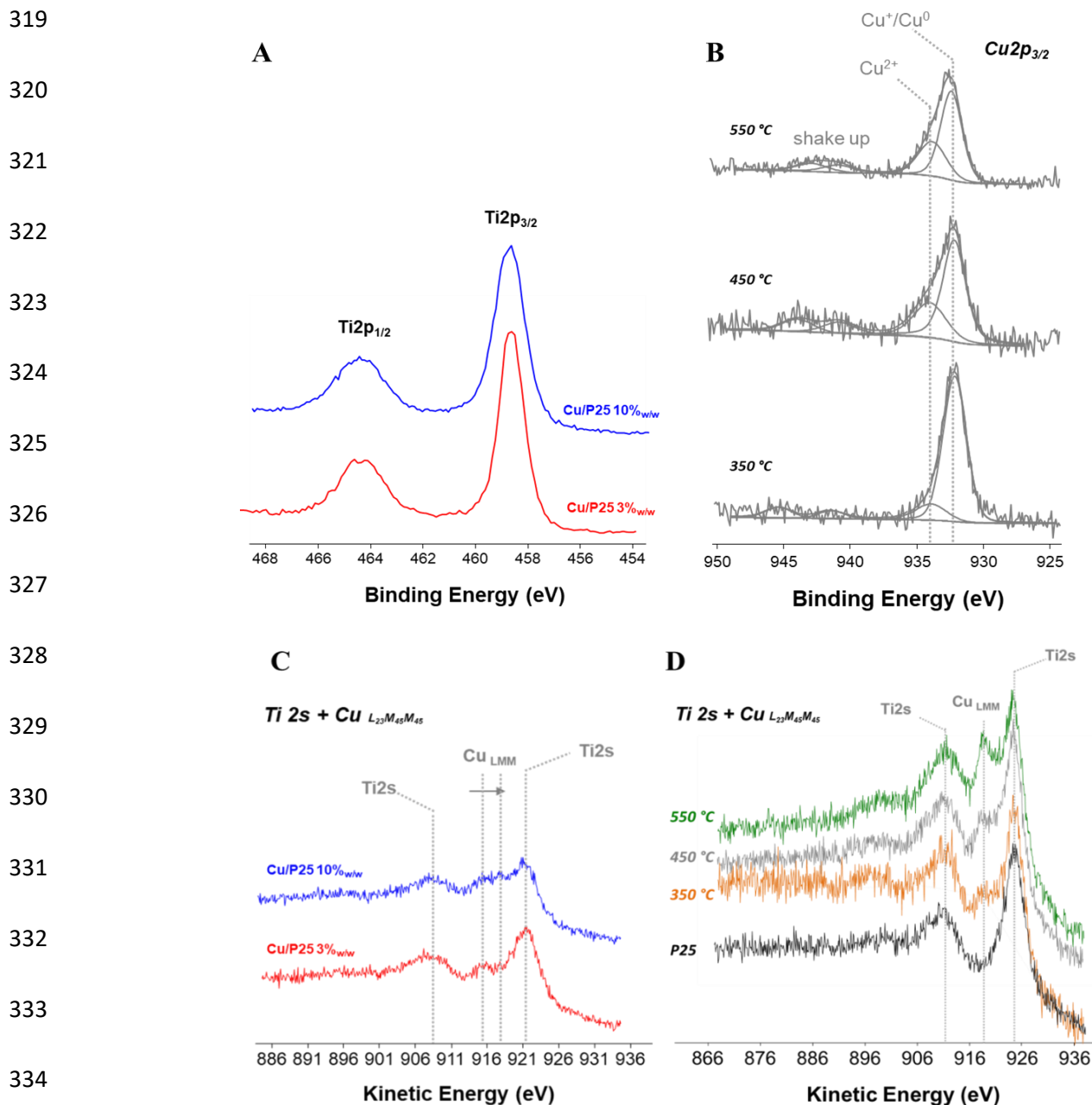
291 Therefore, XRD, EPR and Raman analyses confirm the presence of CuO in Cu/P25 samples.
292 Morphology, crystal structure and copper oxidation states were also assessed through TEM analyses.
293 Figure 3A shows HR-TEM and Fast Fourier Transform (FFT) analyses for fresh Cu(3%)/P25 sample
294 calcined at $350\text{ }^\circ\text{C}$. An interplane distance of $d_{\text{Cu}} = 0.231\text{ nm}$ calculated from the HR-TEM micrograph
295 (Figure 3A), corresponding to the (111) plane of CuO, further confirmed its presence on TiO_2 (d_{TiO_2}
296 $= 0.33\text{ nm}$), in accordance with XRD, Raman and EPR results. Moreover, FFT image (*inset* of Figure
297 3C) clearly justified the existence of TiO_2 material in amorphous structure with some clear spots
298 related to the co-existed CuO particles.



299

300 **Figure 3** - HR-TEM for fresh Cu(3%)/P25 sample calcined at 350 °C (A, inset: FFT analysis) and
 301 for fresh Cu(10%)/P25 catalyst calcined at 350 °C (B, inset: FFT analysis).
 302

303 Changing Cu composition in Cu/P25 catalyst to 10% while maintaining the calcination temperature
 304 at 350 °C did not lead to a significant alteration in the catalyst structure (Figure 3B), however larger
 305 surface deposits were appreciated (Figure 3B). To further clarify the oxidation state of surface Cu-
 306 species, samples were analyzed by means of XPS analysis. Higher temperatures led to an increase of
 307 copper surface availability, as evident from Cu/Ti atomic ratio in Cu(3%)/P25 samples (Table S2).
 308 At 550 °C aggregation phenomena of copper particles can occur, resulting in higher Cu detected
 309 amount in the same analyzed spot. A similar trend is shown when the catalysts were prepared with
 310 increasing bulk copper loading, even at the lowest calcination temperature (Table S3). Actually, both
 311 the total copper increase and the eventual surface aggregation phenomena could contribute to the
 312 increase of copper amount detected on the surface. Indeed, the observed increase in Cu surface
 313 availability was not proportional to the overall Cu content; actual difference between them got wider
 314 with increasing copper loading, suggesting a different size distribution of copper species on TiO₂
 315 surface. Apart from total surface copper availability, XPS measurements were aimed at elucidating
 316 Cu and Ti oxidation state of Ti on TiO₂ surface. Figure 4A shows Ti2p XP spectral region of fresh
 317 Cu(3%)/P25 and Cu(10%)/P25 catalysts. XPS spectra of all catalysts with different copper loadings
 318 are reported in Figure S5.



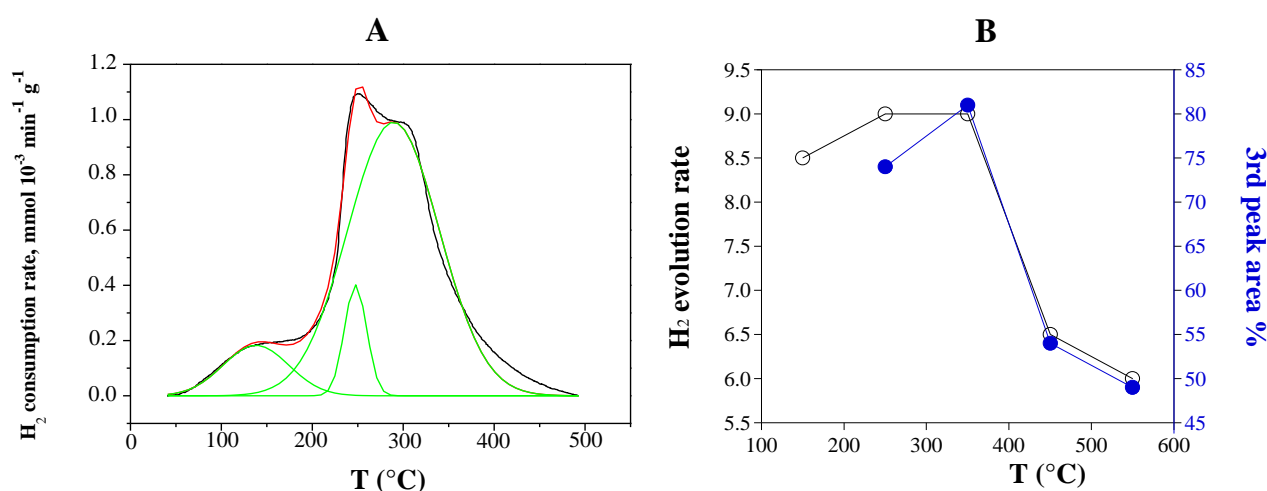
335 **Figure 4** - Ti2p XP spectra of the fresh Cu(3%)/P25 and Cu(10%)/P25 catalysts calcined at 350 °C
 336 (A). Cu2p_{3/2} XP spectra of the fresh Cu(3%)/P25 sample at different calcination temperatures (B).
 337 Ti2s XP+Cu_{LMM} XAE spectra of Cu(3%)/P25 and Cu(10%)/P25 calcined at 350 °C (C) and of
 338 Cu(3%)/P25 at different calcination temperatures (D).

339
 340 In all the spectra, the characteristic peaks of Ti2p_{3/2} and Ti2p_{1/2} were observed at BE values of
 341 458.7±0.1 eV and 464.4±0.1 eV, respectively, and were assigned to Ti⁴⁺ in TiO₂ [1]. A possible
 342 interaction between Cu species and P25 would result not only in the BE shift but also in the change
 343 of the spin-orbit splitting value in the Ti2p signal [1]. Nevertheless, no significant variation was

344 observed neither changing the copper loading nor increasing the calcination temperature (Figure 4A,
345 Figure S5 in Supplementary Information); the value was measured to be constant and equal to 5.7
346 eV, therefore no Cu incorporation into the TiO₂ lattice could be hypothesized [2]. Figure 4B reports
347 Cu2p_{3/2} XP spectra of the Cu(3%)/P25 catalyst calcined at different calcination temperatures. After
348 curve-fitting procedures, the main peak was identified at BE=932.4±0.1eV in all the cases and was
349 ascribed to Cu⁺/Cu⁰ species [1,3]. Furthermore, shake up satellites were visible (940-945 eV) along
350 with a peak at 934.0±0.1eV, that was assigned to Cu²⁺ species [1,3]. The copper spectral regions of
351 the catalysts prepared at higher bulk copper loadings (Figure 4A, Figure S5) as well as at different
352 calcination temperatures (Figure 4B) showed similar results. Particularly, for Cu(3%)/P25 sample at
353 different temperatures, a main peak due to Cu⁺/Cu⁰ species along with variable amounts of Cu²⁺,
354 depending on the Cu loading, was detected (Figure 4B). Since the binding energies of Cu⁺ and Cu⁰
355 are not distinguishable based on Cu2p_{3/2} XP peak, the spectral region relative to X-ray excited Auger
356 copper spectra (XAES Cu_{LMM}) was investigated to fully elucidate the oxidation state of the reduced
357 copper species. Figure 4 reports Cu_{LMM} spectra for fresh Cu(3%)/P25 and Cu(10%)/P25 samples
358 treated at 350 °C (C) and 3%Cu bulk loading at different calcination temperatures (D) .

359 A further challenge in the Cu⁺/Cu⁰ discrimination was represented from the partial overlapping of
360 Cu_{LMM} and the predominant Ti2s spectral regions (black line in Figure 4D). Nevertheless, the main
361 peak for copper was still detectable in all the samples and was found at KE=916.3±0.3 eV. Moreover,
362 the Auger parameter – the sum of the binding energy from XPS and the kinetic energy from XAES –
363 was calculated to be 1848.7±0.1 eV. Both the values demonstrated that the Cu⁺/Cu⁰ peak is ascribable
364 to Cu⁺ species [3]. However, the absence of Cu⁰ traces could not be completely ruled out under these
365 experimental conditions, since the peak would fall at KE=918.6 ±0.2 eV, overlapped with Ti2s peak
366 [41]. Similar results were obtained for XPS spectra of the samples at different calcination
367 temperatures (Figure 4D). When the relative abundance of Cu²⁺ is increased, the peak is shifted to
368 slightly higher KE values, according to KE values for oxidized copper species (Figure 4C) [3].

369 To get a greater insight into the Cu-TiO₂ interaction as function of the annealing temperature, the
 370 reducibility of the samples was studied by means of the TPR technique. The TPR profile of
 371 Cu(3%)/P25 sample after calcination at 350 °C is shown in Figure 5A, while the TPR profiles of
 372 Cu(3%)/P25 sample after calcination at 250, 450 and 550 °C are reported in Figure S6
 373 (Supplementary Information). All of them are reported in the temperature range characteristic of
 374 copper oxide reduction [14, 30, 44], where instead TiO₂ reduction was hardly observed.



375 **Figure 5 – Panel A:** TPR profile of Cu(3%)/P25 sample calcined at 350 °C. **Panel B:** H₂ evolution
 376 rate (○) and percentage of TPR 3rd peak area (●) as a function of calcination temperature for
 377 Cu(3%)/P25 sample.
 378
 379

380 As indicated by the curve fit analysis, the samples showed a distribution of copper species;
 381 conversely, the unsupported CuO showed a single peak at 400 °C [42,43]. The hydrogen consumption
 382 relative to each fitting peak for Cu(3%)/P25 is listed in Table 2 and Table S4 along with T_{max} values.

| Sample | T _{max} (°C) | Hydrogen consumption (μmol/g) |
|------------|-----------------------|-------------------------------|
| Cu(3%)/P25 | 138, 246, 290 | 101, 76, 759 |

383 **Table 2 - Results of TPR measurements for fresh Cu(3%)/P25 sample calcined at 350 °C**
 384

385 The assignment of the reduction peak at lower temperature is quite controversial: it is generally
 386 ascribed to the reduction of highly reducible Cu²⁺ species, though the presence of Cu⁺ species cannot
 387 be ruled out [30]. Indeed, Chen et al. [14] assigned the TPR peak in this range to the reduction of Cu⁺

388 species in Cu(3%)/P25 sample. The formation of Cu⁺ species was ascribed to the presence of oxygen-
389 defect vacancies in the TiO₂ structure. The presence of isolated Cu⁺ species and small Cu₂O cluster
390 with reduction peak at 157 °C and 208 °C, respectively was also proposed by Minsu Jung et al.
391 [44,45].

392 Samples treated at 250 °C and 350 °C, *i.e.* Cu(3%)/P25_250 and Cu(3%)/P25_350, showed the
393 highest hydrogen consumption in correspondence of the peak at about 280-290 °C associable to small
394 and/or highly dispersed CuO particles. TPR profile gradually changed by increasing the calcination
395 temperature, leading to a decrease of the peak at 280-290 °C and to the occurrence of another
396 reduction peak at higher temperature. Peaks located in the 320-400 °C temperature range are
397 indicative of the formation of bulky CuO species [42,43]. Thus, it can be inferred that a lower
398 calcination temperature resulted in a better dispersion of copper species on the support. As far as the
399 overall H₂ consumption is concerned, it was much higher with respect to the stoichiometric amount
400 as calculated under the hypothesis of the occurrence of all Cu as Cu²⁺ species. This likely indicated
401 some spillover phenomena of H₂ occurring over the support with the likely partial reduction of the
402 latter, as generally observed for copper doped anatase [46].

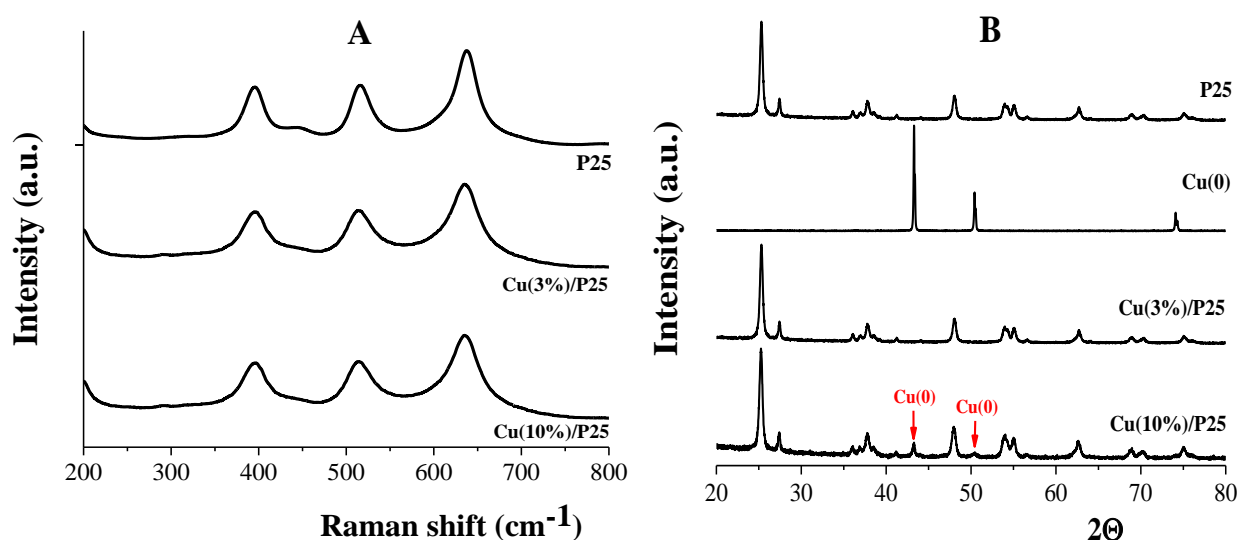
403 The influence of calcination temperature on hydrogen production rate is reported in Figure 5B,
404 together with the percentage of amount of the third peak area in TPR analysis. Actually, evolved H₂
405 amount appeared closely related to the fraction of highly dispersed CuO particles strongly interacting
406 with the support, probably accounting for the third peak area in TPR analysis (Table 2 and Table S4).

407

408 **3.3 Characterization of the used Cu/P25 photocatalysts**

409 The Cu/P25 catalysts were also analyzed after their use to assess any evolution of Cu oxidative state
410 during photocatalytic runs, so as to identify the nature of Cu-active species towards H₂ evolution as
411 well as their role in photocatalytic. Particularly, this investigation was carried out on both
412 Cu(3%)/P25 and Cu(10%)/P25 samples, calcined at 350 °C. Specifically, Raman spectra of both

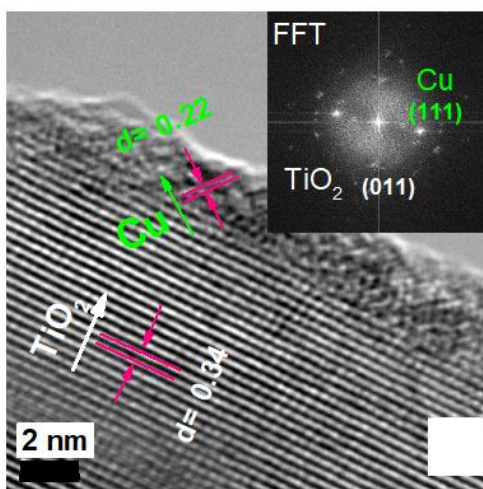
413 samples after photocatalytic run, reported in Figure 6A, indicated that no peak ascribable to the
 414 presence of cupric species was observed. This result was also confirmed by the EPR evidence
 415 indicating that these considered samples did not show any paramagnetic signal. Since no significant
 416 release of cupric ions was appreciated during photoreforming tests, obtained results suggest the
 417 reduction of the copper during the photoreforming process. Actually, the indigo color of the final
 418 suspension supported a change of the oxidation state of copper deposited on titania, further confirmed
 419 by XRD diffraction analysis too. Notably, XRD patterns of used Cu(10%)/P25 collected after the
 420 photocatalytic run, no longer showed diffraction peaks of CuO phase and clearly indicated the
 421 presence of Cu(0) diffraction peaks (Figure 6B). Unfortunately, due to the low Cu content, this peak
 422 was not detectable in the XRD spectrum of the used Cu(3%)/P25 sample.



423
 424 **Figure 6 – Panel A:** Raman spectra of bare P25, used Cu(3%)/P25 and Cu(10%)/P25 samples
 425 calcined at 350 °C for 5h. **Panel B:** XRD patterns of bare P25, Cu(0), used Cu(3%)/P25 and
 426 Cu(10%)/P25 calcined at 350 °C for 5h.

427
 428 HR-TEM and FFT analyses were performed on used Cu(3%)/P25 catalyst calcined at 350 °C, showing
 429 co-existence of Cu₂O and Cu⁰ on the TiO₂ particles, thus indicating CuO reduction (Figures 7) during
 430 the photocatalytic experiment. It is noteworthy mentioning the co-existence of Cu₂O and Cu⁰ in the
 431 used Cu/P25 catalysts was deduced from the indicated face (111) that corresponds to both Cu₂O and

432 Cu^0 [47], the latter also confirmed by XRD analysis. Again, Cu_2O (111) and Cu^0 (111) were the
433 dominant copper species in the 10%Cu-containing catalyst (Figure S7).



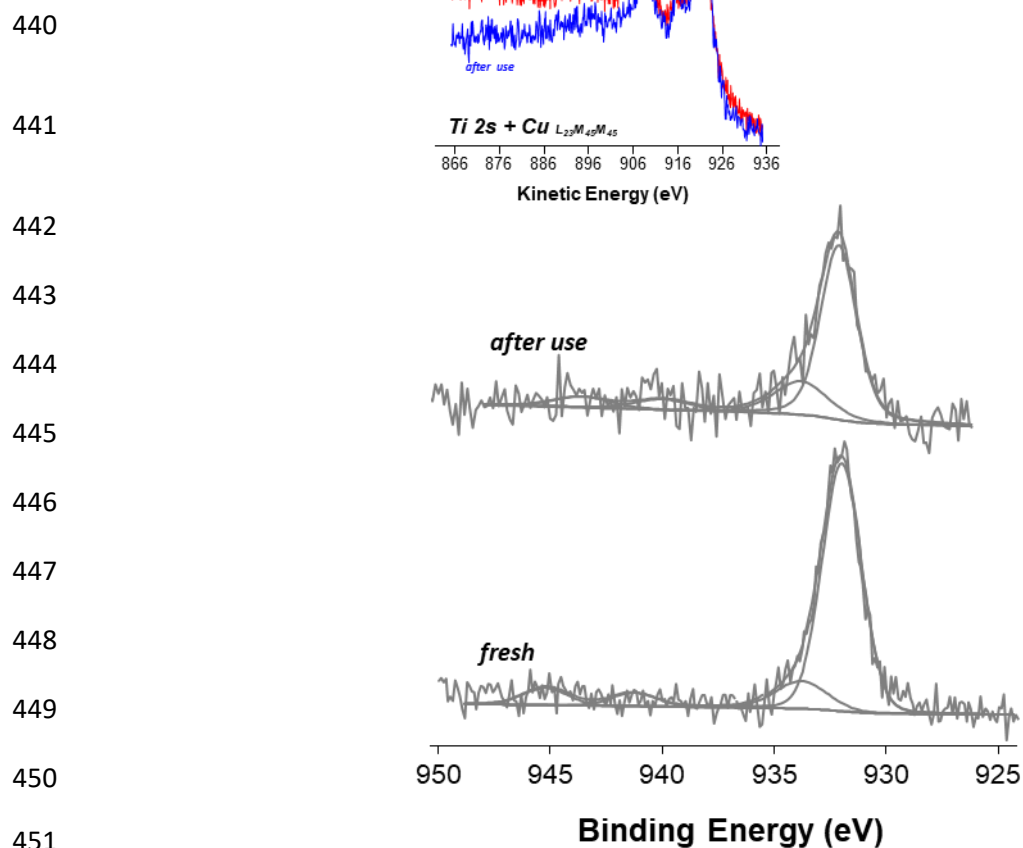
434

435 **Figure 7** - HR-TEM for used Cu(3%)/P25 sample calcined at 350 °C.

436

437 The comparison of XPS copper spectra of Cu(3%)/P25 before and after use are reported in Figure 8
438 while Cu/Ti ratio for the same samples are reported in Table S5 (Supplementary Information).

439

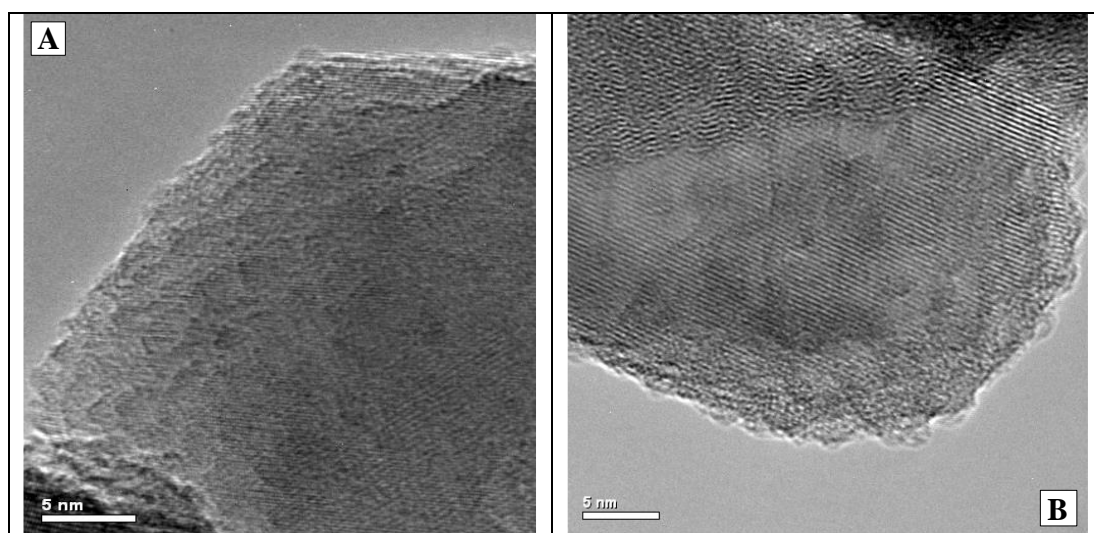


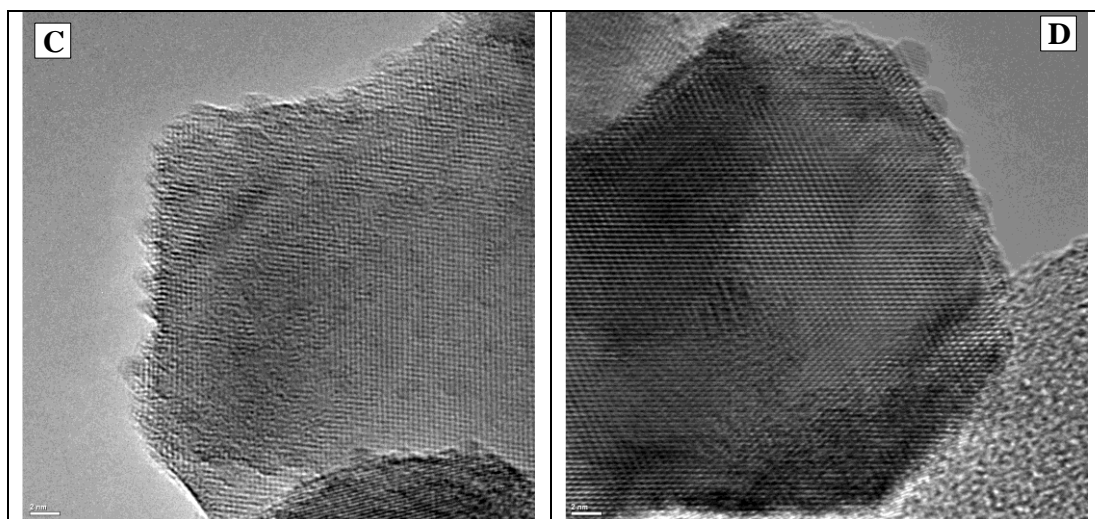
453 **Figure 8** - Cu_{2p_{3/2}} XP spectra for Cu(3%)/P25_350°C fresh and after use. Corresponding Cu_{LMM}
 454 XAE spectra in the inset.

455
 456 From XPS and XAES results no specific differences could be derived on the surface of the catalyst
 457 before and after use. Both spectra presented a small amount of Cu²⁺ (peak at BE=, 934.0±0.1eV,
 458 along with shake up features) and the predominant Cu⁺/Cu⁰ oxidation state on the catalyst's surface
 459 (main peak at BE=932.4±0.1eV). Moreover, XAES peaks are completely overlapped. Furthermore,
 460 Cu⁰ peak, if any, is overlapped with Ti_{2s} peak in XAE spectrum: this makes any possible change in
 461 Cu⁰ amount hardly appreciable in the studied systems [41]. Finally, Cu/Ti ratio slightly increased
 462 after use (Table S5), probably due a different distribution of surface copper species.

463 Despite Cu-doped TiO₂ have been intensively studied for H₂ production through photo-reforming,
 464 published results are still controversial on the activity of different Cu oxidation states [12, 18-26].
 465 Our results clearly showed that calcination of Cu(NO₃)₂×3H₂O-impregnated P25 samples under
 466 nitrogen atmosphere leads to a mixture of CuO and Cu₂O nanostructures on P25 surface. The former

467 was clearly evidenced by bulk characterization techniques, in particular EPR and Raman
468 spectroscopy. Furthermore, XPS analysis proved the presence of surface Cu_2O as the predominant
469 CuO_x species. The poor CuO amount measured through this methodology, can be explained
470 considering this technique revealing composition of the more exposed layer on the surface. These
471 results supported earlier reports, where both oxidation states are observed for copper [14, 16-20, 28].
472 Furthermore, as a major point, from TPR analysis different populations of CuO_x species could be
473 distinguished on the catalysts. A highly dispersed fraction of small and dispersed CuO particles
474 strongly interacting with the support was appreciated on the catalysts with the highest H_2 evolution
475 rate. During photocatalytic process, CuO_x based deposits were reduced to $\text{Cu}_2\text{O}/\text{Cu}^0$ and concurrently
476 a morphological evolution was also appreciated (Figure 9). Notably, broadened deposits with less
477 defined morphology were observed in Cu(3%)/P25 sample after use, while larger CuO_x surface
478 deposits were observed in Cu(10%)/P25 sample. Previous reports provided evidence of Cu^{2+}
479 reduction to Cu^+ [19, 33] and to Cu^0 [33] under UVA irradiation; however, even this aspect is still
480 debated.
481





482

483 **Figure 9** - HR-TEM for Cu(3%)/P25 sample fresh (A) and after used (B) and for Cu(10%)/P25
 484 sample, (C) and after used (D).

485

486 Experimental findings and in particular morphological evolution from HR-TEM analysis as well as
 487 Cu changes in copper surface availability after use (Table S5, Supplementary Information) suggested
 488 that CuO_x species undergo in situ dynamic nanostructuring during photocatalytic run. The process is
 489 driven by the dissolution-redeposition of CuO_x deposits on the TiO₂ surface under UV irradiation
 490 [48]. In more detail, CuO_x species must be involved in a dissolution process, leading to Cu²⁺ ions,
 491 that upon illumination are reduced to Cu₂O and then to Cu, by photo-generated electrons, according
 492 to the following equations, both involving dissolved Cu ions:

493

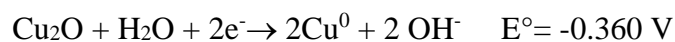


494



495 In fact, electrochemical potentials of both semi-reactions are higher than H⁺ species, supporting the
 496 hypothesis of Cu²⁺ and Cu⁺ preferential reduction by TiO₂ photogenerated electrons. The excess of
 497 electrons in the Cu deposits, accompanied by the consumption of photogenerated holes by methanol,
 498 allowed for the deposits to keep a metallic state throughout the reaction, as experimentally
 499 ascertained. Actually, negative electrochemical potential of solid state reduction

500



501 further supports the hypothesis of reduction from solution.

502 Indeed, Cu_2O reduction to metallic Cu was not revealed by previous studies on Cu impregnated TiO_2

503 [19], however these differences should depend on the size of CuO_x deposits and their interaction with

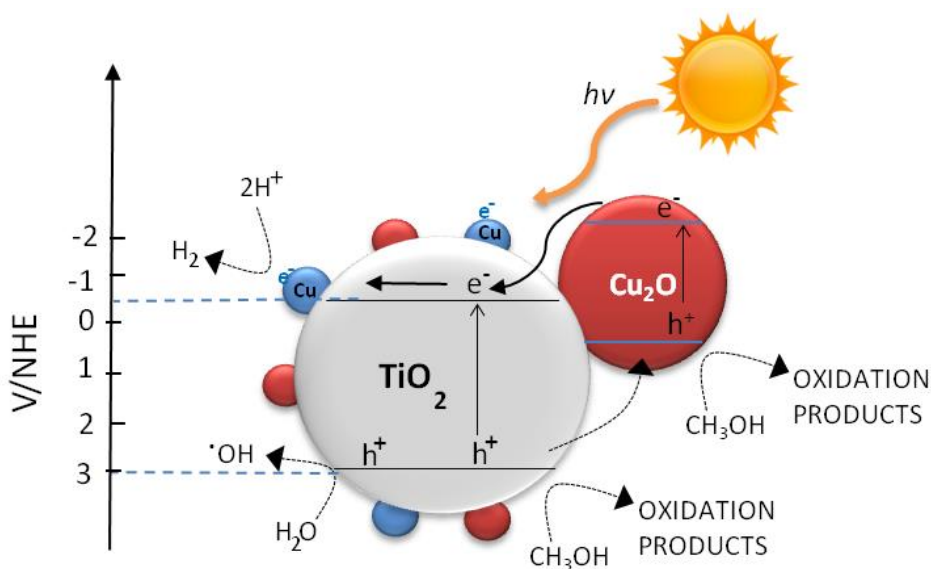
504 TiO_2 surface, strongly influencing their reducibility.

505 Actually, change in size and distribution of Cu species on the surface, as evidenced by HR-TEM,

506 supports this mechanism. Metallic Cu nanoparticles, should act as a co-catalyst for H_2 production,

507 attracting photogenerated electrons from TiO_2 and promoting their transfer to the protons [19],

508 according to the scheme in Figure 10.



509

510 **Figure 10** - Proposed hydrogen photogeneration mechanism for Cu/ Cu_2O / TiO_2 system.

511

512 At the same time, upon illumination, Cu_2O should inject photoelectrons into TiO_2 conduction band

513 and hosting holes from TiO_2 valence band (Figure 10). Electrons injected into TiO_2 bands should be

514 involved in H^+ reduction, thus accounting for H_2 production since the beginning of the photocatalytic

515 run. The increased presence of holes in Cu_2O may limit further reduction of the Cu^+ to Cu^0 as well as

516 methanol oxidation, thus accounting for constant pH values during photo-reforming. Both processes

517 restrict electron/hole recombination phenomena and account for improved photocatalytic activity of

518 Cu doped P25 [19].

519

520 **4. Conclusions**

521 Altogether, our photocatalytic tests and the in-depth investigation on impregnated Cu/P25 systems
522 elucidated the nature of copper species active in hydrogen production on Cu/P25 systems. Our
523 findings showed that:

524 1) Both CuO and Cu₂O nanostructures were obtained onto Cu/P25 by impregnation and further heat
525 treatment in nitrogen.

526 2) The sample allowing the highest H₂ production rates showed the highest fraction of finely
527 dispersed CuO nanostructures, that during the photocatalytic process, CuO_x species undergo an
528 in situ dynamic nanostructuring, leading to a significant change in both oxidation state and size
529 distribution. This evolution is probably based on a dissolution-redeposition process. In particular,
530 CuO_x species were involved in a dissolution process, followed by reduction of Cu²⁺ ions to Cu⁺
531 and Cu⁰ by photo-generated electrons.

532 3) Both Cu₂O and Cu⁰ acted as co-catalysts for H₂ generation. Upon illumination, the former
533 injected photoelectrons into TiO₂ conduction band. The latter acted as a co-catalyst, hosting
534 photogenerated electrons from TiO₂ and mediating their transfer to the protons. Both processes
535 restricted electron/hole recombination phenomena and accounted for improved photocatalytic
536 activity of Cu doped P25.

537 The obtained findings clearly outline Cu/P25 catalysts as complex and dynamic systems. Their
538 evolution during photocatalytic process must be influenced by solution properties as well as by
539 preparation conditions of the catalyst itself, that markedly affect both size distribution and dispersion
540 of Cu species, and ultimately lead to different ratios between copper oxidation states on the catalyst
541 surface, thus affecting H₂ production rate.

542 The present work highlights that in situ catalysts transformation could improve their performance,
543 lying the basis to explore this strategy to optimize activity of other catalytic systems.

544

545 **References**

- 546 (1) G. Colon, Towards the hydrogen production by photocatalysis, *Appl. Catal. A* 518 (2016) 48–
547 59. <https://doi.org/10.1016/j.apcata.2015.11.042>
- 548 (2) A.V. Puga, Photocatalytic production of hydrogen from biomass-derived feedstocks, *Coord.*
549 *Chem. Rev.* 315 (2016) 1–66. <https://doi.org/10.1016/j.ccr.2015.12.009>
- 550 (3) J. M. Valero, S. Obregón, G. Colón, Cu–TiO₂ systems for the photocatalytic H₂ production:
551 Influence of structural and surface support features, *Appl. Catal. B Environmental* 179 (2015)
552 468-478. <https://doi.org/10.1016/j.apcatb.2015.05.043>
- 553 (4) R. A. Rather, S. Singh, B. Pal, A Cu⁺¹/Cu⁰-TiO₂ mesoporous nanocomposite exhibits improved
554 H₂ production from H₂O under direct solar irradiation, *J.Catal.* 346 (2017) 1–9.
555 <https://doi.org/10.1016/j.jcat.2016.11.021>
- 556 (5) T. Montini, M. Monai, A. Beltram, I. Romero-Ocaña, P. Fornasiero, H₂ production by
557 photocatalytic reforming of oxygenated compounds using TiO₂-based materials, *Mater. Sci.*
558 *Semicond. Process.* 42 (2016) 122–130. <https://doi.org/10.1016/j.mssp.2015.06.069>
- 559 (6) M. Hinojosa-Reyes, R. Camposeco-Solís, R. Zanella, V. Rodríguez González, Hydrogen
560 production by tailoring the brookite and Cu₂O ratio of sol-gel Cu-TiO₂ photocatalysts,
561 *Chemosphere* 184 (2017) 992-1002. <https://doi.org/10.1016/j.chemosphere.2017.06.066>
- 562 (7) M. R. Pai, A. M. Banerjee, S. A. Rawool, A. Singhal, C. Nayak, S. H. Ehrman, A. K. Tripathi,
563 S. R. Bharadwaj, A comprehensive study on sunlight driven photocatalytic hydrogen generation
564 using low cost nanocrystalline Cu-Ti oxides, *Solar Energy Materials & Solar Cells* 154 (2016)
565 104-120. <https://doi.org/10.1016/j.solmat.2016.04.036>
- 566 (8) D. Guerrero-Araque, P. Acevedo-Peña, D. Ramírez-Ortega, H. A. Calderon, R. Gomez, Charge
567 transfer processes involved in photocatalytic hydrogen production over CuO/ZrO₂-TiO₂
568 materials, *Int. J. Hydrogen Energ.* 42 (2017) 9744-753.
569 <https://doi.org/10.1016/j.ijhydene.2017.03.050>
- 570 (9) L. Clarizia, D. Spasiano, I. Di Somma, R. Marotta, R. Andreozzi, D.D. Dionysiou, Copper
571 modified-TiO₂ catalysts for hydrogen generation through photoreforming of organics. A short
572 review, *Int. J. Hydrogen Energ.* 39 (2014) 16812-16831.
573 <https://doi.org/10.1016/j.ijhydene.2014.08.037>
- 574 (10) A.J.J. Lennox, P. Bartels, M.M. Pohl, H. Junge, M. Beller, *In situ* photodeposition of copper
575 nanoparticles on TiO₂: Novel catalysts with facile light-induced redox cycling, *J. Catal.* 340
576 (2016) 177–183. <https://doi.org/10.1016/j.jcat.2016.04.011>

- 577 (11) Z. He, J. Fu, B. Cheng, J. Yu, S. Cao, $\text{Cu}_2(\text{OH})_2\text{CO}_3$ clusters: Novel noble-metal-free
578 cocatalysts for efficient photocatalytic hydrogen production from water splitting, *Appl. Catal.*
579 *B* 205 (2017) 104–111. <https://doi.org/10.1016/j.apcatb.2016.12.031>
- 580 (12) L.S. Yoong, F.K. Chong, Binay K. Dutta, Development of copper-doped TiO_2 photocatalyst
581 for hydrogen production under visible light, *Energy* 34 (2009) 1652–1661.
582 <https://doi.org/10.1016/j.energy.2009.07.024>
- 583 (13) C. S. Chen, J. H. You, J. H. Lin, Y. Y. Chen, Effect of highly dispersed active sites of
584 Cu/TiO_2 catalyst on CO oxidation, *Catalysis Communications* 9 (2008) 2381–2385.
585 <https://doi.org/10.1016/j.catcom.2008.06.003>
- 586 (14) C. S. Chen, T. C. Chen, C. C. Chen, Y. T. Lai, J. H. You, T. M. Chou, C. H. Chen, J. F. Lee,
587 Effect of Ti^{3+} on TiO_2 -Supported Cu Catalysts Used for CO Oxidation, *Langmuir* 28 (2012)
588 9996–10006. <https://doi.org/10.1021/la301684h>
- 589 (15) F. Boccuzzi, A. Chiorino, G. Martra, M. Gargano, N. Ravasio, B. Carrozzini, Preparation,
590 Characterization, and Activity of Cu/TiO_2 Catalysts. I. Influence of the Preparation Method on
591 the Dispersion of Copper in Cu/TiO_2 , *J. Catal.* 165 (1997) 129–39.
592 <https://doi.org/10.1006/jcat.1997.1475>
- 593 (16) F. Coloma, F. Marquez, C. H. Rochester, Determination of the nature and reactivity of copper
594 sites in Cu-TiO_2 catalysts, *J. A. Anderson, Phys. Chem. Chem. Phys.* 2 (2000) 5320–5327.
595 <https://doi.org/10.1039/B005331G>
- 596 (17) G. Wu, N. Guan, L. Li, Low temperature CO oxidation on $\text{Cu-Cu}_2\text{O/TiO}_2$ catalyst prepared
597 by photodeposition, *Catal. Sci. Technol.* 1 (2011) 601–608. <https://doi.org/10.1039/C1CY00036E>
- 598 (18) K. Lalitha, G. Sadanandam, V D Kumari, M Subrahmanyam, B Sreedhar, N Y Hebalkar, Highly
599 Stabilized and Finely Dispersed $\text{Cu}_2\text{O/TiO}_2$: A Promising Visible Sensitive Photocatalyst for
600 Continuous Production of Hydrogen from Glycerol:Water Mixtures, *J. Phys. Chem. C* 114
601 (2010) 22181–22189. <https://doi.org/10.1021/jp107405u>
- 602 (19) M. Jung, J. N. Hart, J Scott, Y H Ng, Y Jiang, R Amal, Exploring Cu oxidation state on TiO_2 and
603 its transformation during photocatalytic hydrogen evolution, *Appl. Catal. A: General* 521
604 (2016) 190–201. <https://doi.org/10.1016/j.apcata.2015.11.013>
- 605 (20) A. Heciak, A. W. Morawski, B. Grzmil, S. Mozia, Cu-modified TiO_2 photocatalysts for
606 decomposition of acetic acid with simultaneous formation of $\text{C}_1\text{-C}_3$ hydrocarbons and
607 hydrogen, *Appl. Catal. B: Environmental* 140–141 (2013) 108–114.
608 <https://doi.org/10.1016/j.apcatb.2013.03.044>

- 609 (21) A. J. Simamora, T. L. Hsiung, F. C. Chang, T. C. Yang, C. Y. Liao, H. P. Wang, Photocatalytic
610 splitting of seawater and degradation of methylene blue on CuO/nano TiO₂, *Int. J. Hydrogen*
611 *Energy* 37 (2012) 13855–8. <https://doi.org/10.1016/j.ijhydene.2012.04.091>
- 612 (22) J. Yu, Y. Hai, M. Jaroniec, Photocatalytic hydrogen production over CuO-modified titania, *J.*
613 *Coll. Interf. Sci.* 357 (2011) 223–228. <https://doi.org/10.1016/j.jcis.2011.01.101>
- 614 (23) L. Li, L. Xu, W. Shi, J. Guan, Facile preparation and size-dependent photocatalytic activity of
615 Cu₂O nanocrystals modified titania for hydrogen evolution, *Int. J. Hydrogen Energy* 38 (2013)
616 816–822. <https://doi.org/10.1016/j.ijhydene.2012.10.064>
- 617 (24) J. Bandara, C.P.K. Udawatta, C.S.K. Rajapakse, Highly stable CuO incorporated
618 TiO₂ catalyst for photocatalytic hydrogen production from H₂O, *Photochem. & Photobiol. Sci.*
619 4 (2005) 857–861. <https://doi.org/10.1039/B507816D>
- 620 (25) S. Xu, D. D. Sun, Significant improvement of photocatalytic hydrogen generation rate over
621 TiO₂ with deposited CuO, *Int. J. Hydrogen Energy* 34 (2009) 6096–6104.
622 <https://doi.org/10.1016/j.ijhydene.2009.05.119>
- 623 (26) S. Xu, J. Ng, X. Zhang, H. Bai, D. D. Sun, Fabrication and comparison of highly efficient Cu
624 incorporated TiO₂ photocatalyst for hydrogen generation from water, *Int. J. Hydrogen Energy*
625 35 (2010) 5254–5261. <https://doi.org/10.1016/j.ijhydene.2010.02.129>
- 626 (27) P. Khemthong, P. Photai, N. Grisdanurak, Structural properties of CuO/TiO₂ nanorod in
627 relation to their catalytic activity for simultaneous hydrogen production under solar light, *Int.*
628 *J. Hydrogen Energy* 38 (2013) 15992–16001. <https://doi.org/10.1016/j.ijhydene.2013.10.065>
- 629 (28) A.L. Luna, M.A. Valenzuela, C. Colbeau-Justin, P. Vázquez, J.L. Rodriguez, J.R. Avendaño,
630 S. Alfaro, S. Tirado, A. Garduño, J.M. De la Rosa, Photocatalytic degradation of gallic acid
631 over CuO–TiO₂ composites under UV/Vis LEDs irradiation, *Appl. Catal. A: General* 521 (2016)
632 140–148. <https://doi.org/10.1016/j.apcata.2015.10.044>
- 633 (29) Z. Xi, C. Li, L. Zhang, M. Xing, J. Zhang, Synergistic effect of Cu₂O/TiO₂ heterostructure
634 nanoparticle and its high H₂ evolution activity, *Int. J. Hydrogen Energy* 39 (2014) 6345–6353.
635 <https://doi.org/10.1016/j.ijhydene.2014.01.209>
- 636 (30) J.M. Valero, S. Obregón, G. Colón, Active Site Considerations on the Photocatalytic
637 H₂ Evolution Performance of Cu-Doped TiO₂ Obtained by Different Doping Methods, *ACS*
638 *Catal.* 4 (2014) 3320–3329. <https://doi.org/10.1021/cs500865y>
- 639 (31) M. Jung, J. Scott, Y.H. Ng, Y. Jiang, R. Amal, CuO_x dispersion and reducibility on TiO₂ and
640 its impact on photocatalytic hydrogen evolution, *Int. J. Hydrogen Energy* 39 (2014) 12499–
641 12506. <https://doi.org/10.1016/j.ijhydene.2014.06.020>

- 642 (32) L. Clarizia, G. Vitiello, D. K. Pallotti, B. Silvestri, M. Nadagouda, S. Lettieri, G. Luciani, R.
643 Andreozzi, P. Maddalena, R. Marotta, Effect of surface properties of copper-modified
644 commercial titanium dioxide photocatalysts on hydrogen production through photoreforming
645 of alcohols, *Int. J. Hydrogen Energy* 42 (2017) 28349-28362.
646 <https://doi.org/10.1016/j.ijhydene.2017.09.093>
- 647 (33) D. M. Tobaldi, N. Rozman, M. Leoni, M. P. Seabra, A. S. Škapin, R. C. Pullar, J. A. Labrincha,
648 Cu–TiO₂ Hybrid Nanoparticles Exhibiting Tunable Photochromic Behavior, *J. Phys. Chem. C*
649 119 (2015) 23658. <https://doi.org/10.1021/acs.jpcc.5b07160>
- 650 (34) T.H. Fleisch, G. J. Mains, Reduction of copper oxides by UV radiation and atomic hydrogen
651 studied by XPS, *Application of Surface Science* 10 (1982) 51-62. [https://doi.org/10.1016/0378-](https://doi.org/10.1016/0378-5963(82)90134-9)
652 [5963\(82\)90134-9](https://doi.org/10.1016/0378-5963(82)90134-9)
- 653 (35) P. Cheng, W. Li, T. Zhou, Y. Jin, M. Gu, Physical and photocatalytic properties of zinc ferrite
654 doped titania under visible light irradiation, *J. Photochem. Photobiology A Chem.* 168 (2004)
655 97–10. <https://doi.org/10.1016/j.jphotochem.2004.05.018>
- 656 (36) A. Compaan, H. Z. Cummins, Raman Scattering, Luminescence, and Exciton-Phonon Coupling
657 in Cu₂O, *Phys. Rev. B*, 6 (1972) 4753. <https://doi.org/10.1103/PhysRevB.6.4753>
- 658 (37) H. F. Goldstein, Dai-sik Kim, Peter Y. Yu, L. C. Bourne, J-P. Chaminade, L. Nganga, Raman
659 study of CuO single crystals, *Phys. Rev. B* 41 (1990) 7192.
660 <https://doi.org/10.1103/PhysRevB.41.7192>
- 661 (38) B. Choudhury, M. Dey, A. Choudhury, Defect generation, *d-d* transition, and band gap
662 reduction in Cu-doped TiO₂ nanoparticles, *Int. Nano Lett.* 3 (2013) 25.
663 <https://doi.org/10.1186/2228-5326-3-25>
- 664 (39) T. Oku, R. Motoyoshi, K. Fujimoto, T. Akiyama, B. Jeyadevan, J. Cuya, Structures and
665 photovoltaic properties of copper oxides/fullerene solar cells, *J. Phys. Chem. Solids* 72 (2011)
666 1206-1211. <https://doi.org/10.1016/j.jpcs.2011.06.014>
- 667 (40) N. Wongpisutpaisan, P. Charoonsuk, N. Vittayakorn, W. Pecharapa, Sonochemical Synthesis
668 and Characterization of Copper Oxide Nanoparticles, *Energy Procedia* 9 (2011) 404-409.
669 <https://doi.org/10.1016/j.egypro.2011.09.044>
- 670 (41) J.F. Moulder, W.F. Stickle, P.E. Sobol, K.D. Bomben, *Handbook of Photoelectron*
671 *Spectroscopy*, Physical Electronics Inc. 1995.
- 672 (42) S. Esposito, M. Turco, G. Bagnasco, C. Cammarano, P. Pernice, A. Aronne, Highly dispersed
673 sol-gel synthesized Cu–ZrO₂ materials as catalysts for oxidative steam reforming of methanol,
674 *Appl. Catal., A* 372 (2010) 48-57. <https://doi.org/10.1016/j.apcata.2009.10.006>

- 675 (43) S. Esposito, M. Turco, G. Bagnasco, C. Cammarano, P. Pernice, New insight into the
676 preparation of copper/zirconia catalysts by sol–gel method, *Appl. Catal., A* 403 (2011) 128-
677 135. <https://doi.org/10.1016/j.apcata.2011.06.024>
- 678 (44) M. Jung, H. Y. Ng, Y. Jiang, J. Scott, R. Amal, Active Cu species in Cu/TiO₂ for photocatalytic
679 hydrogen evolution, In: *Chemeca 2013 (41st : 2013 : Brisbane, Qld.)*. Chemeca 2013:
680 Challenging Tomorrow. Barton, ACT: Engineers Australia, 2013: 214-217.
- 681 (45) G. Wu, N. Guan, L. Li, Low temperature CO oxidation on Cu–Cu₂O/TiO₂ catalyst prepared
682 by photodeposition, *Catal. Sci. & Technol.* 1 (2011) 601-608.
683 <https://doi.org/10.1039/C1CY00036E>
- 684 (46) I. Rossetti, J. Lasso, E. Finocchio, G. Ramis, V. Nichele, M. Signoretto, A. Di Michele, TiO₂-
685 supported catalysts for the steam reforming of ethanol, *Appl. Catal., A* 477 (2014) 42–53.
686 <https://doi.org/10.1016/j.apcata.2014.03.004>
- 687 (47) E. Aslan, I. H. Patir, M. Ersoz, Cu Nanoparticles Electrodeposited at Liquid–Liquid Interfaces:
688 A Highly Efficient Catalyst for the Hydrogen Evolution Reaction, *Chemistry-A European J.* 21
689 (2015) 4585-4589. <https://doi.org/10.1002/chem.201406615>
- 690 (48) D.V. Shinde, Z. Dang, U. Petralanda, M. Palei, M. Wang, M. Prato, A. Cavalli, L. De Trizio
691 and L. Manna, In Situ Dynamic Nanostructuring of the Cu–Ti Catalyst-Support System
692 Promotes Hydrogen Evolution under Alkaline Conditions, *ACS Appl. Mater. Interfaces* 10
693 (2018) 29583–29592. <https://doi.org/10.1021/acsami.8b09493>